Eur. J. Mech. B - Fluids 20 (2001) 275–301

S0997-7546(00)01120-1/FLA

Turbulent transport of a passive scalar in a round jet discharging into a co-flowing stream

Yan Antoine, Fabrice Lemoine *, Michel Lebouché

Laboratoire d'Energétique et de Mécanique Théorique et Appliquée, 2, Avenue de la Forêt de Haye, BP 160, 54504 Vandœuvre-les-Nancy cedex, France

(Received 26 May 2000; revised 21 September 2000; accepted 17 October 2000)

Abstract – The mass transport properties of a round turbulent jet of water discharging into a low velocity co-flowing water stream, confined in a square channel, is investigated experimentally. The measurement region is the self-similar range from $x/d = 70$ to $x/d = 140$. Combined laser-induced fluorescence and 2D laser Doppler velocimetry are used in order to measure simultaneously, instantaneously and in the same probe volume, the molecular concentration of a passive scalar and two components of the velocity. This technique allows the determination of moments involving correlations of both velocity and concentration fields, which are necessary to validate the second-order modelling schemes. Both transport equations of Reynolds shear stress $\overline{uv}$ and turbulent mass flux $\overline{vc}$ have been considered. In both cases, advection, production and diffusion terms have been determined experimentally. The pressure-strain correlation and the pressure scrambling term are inferred with the help of the budget of Reynolds shear stress and mass turbulent transport equations. Second order closure models are evaluated in the light of the experimental data.

The turbulent Schmidt number is found to be almost constant and equal to 0.62 in the center region and decreases strongly to zero in the mixing layer of the jet. The effects of the co-flow on the turbulent mixing process are also highlighted. © 2001 Éditions scientifiques et médicales Elsevier SAS

axisymmetric jet / passive scalar / closure models / turbulent diffusion / laser-induced fluorescence

1. Introduction

The transport of a passive scalar such as concentration in a turbulent flow is an important problem in numerous industrial and natural processes. In many cases, the turbulent flows producing the scalar transport are complex. Mathematical models have been developed in order to predict the dynamical flowfield and the associated mean and fluctuating concentration field. In fact, all the features of the concentration field are of interest: on the one hand the mean distribution of the concentration in the flow, and on the other hand the peak of concentration and its intermitency generated by the turbulent field. Mathematical models in current use have been evaluated and validated with the help of experimental studies and measurements performed on basic flowfields, before being applied to more complex situations. Among the basic well known flowfields, the turbulent round jet is a non-homogeneous shear flow, for which the literature is abundant. This kind of flowfield can reasonably be a base for more complex situations. It can also be added that turbulent mass diffusion in jets appears in numerous industrial situations and in nature.

The more simple turbulence models are based on eddy viscosity coefficient or mixing length schemes and allow us to describe, with reasonable agreement with experimental data, the mean characteristics of flowfields such as turbulent boundary layers, jets or wakes. The more complex $k - \varepsilon$ schemes use transport equations and allow us to predict the mean and turbulent flow parameters. The next step is the development of second-order

* Correspondence and reprints.
E-mail address: flemoine@ensem.inpl-nancy.fr (F. Lemoine).

closure models, which are adequate for the numerical calculation of turbulent shear flows ([1–3]). In these kind of models, correlations between fluctuating quantities representing momentum and mass (or heat) transport are determined by their own transport equations. The model for the Reynolds stress tensor components developed by Launder et al. [2], applied to shear flows, can be mentioned here for example. A calculation of the mean velocity, Reynolds shear stress and normal stress profiles using a second-order closure model has been reported in [2], showing a good agreement between predictions and measurements.

Turbulent round and plane jets are extensively studied in a significant number of articles. Numerous articles concern independent measurements of velocity, concentration or temperature in turbulent plane or round jet. Hinze and Van der Hegge [4] investigated time averaged axial and radial distributions of axial velocity, temperature and gas concentration in an axially symmetrical jet issuing in quiescent air. In this work, the temperature was measured with the use of a thermocouple, velocity being measured by a total-head tube, serving also to take samples of the gas mixture in the jet in order to perform concentration measurements. Wygnanski and Fiedler [5] described extensively the self-preserving zone of a round jet: the mean and fluctuating dynamic flowfield, the turbulent kinetic energy budget, the integral scale and Taylor microscale of turbulence were all detailed. Hussein et al. [6] reported a wide range of experimental results of velocity moments (to third order) in an axisymmetric jet. Stationary, flying hot wire and burst mode LDA techniques were compared. It was shown that reliable results may be obtained with the help of flying hot wire and LDA techniques. The main results concerned the turbulent kinetic energy balance of the jet and the estimation of both pressure-velocity and pressure-strain correlations.

Numerous works on heated jets are available in literature. The use of the combined hot wire anemometry and cold wire thermometry allows simultaneous and instantaneous determination of two velocity components and temperature. Chevray and Tutu [7] performed conditional measurements based on the analysis of the turbulence intermittency and determined the fluctuating temperature field and the temperature-velocity cross-correlations. The authors demonstrated that the majority of the momentum and heat transport can be attributed to the large scale turbulence structures. Chua and Antonia [8] determined, in the self-preserving zone of the jet, the distribution of the Reynolds shear stress, the turbulent heat flux and the turbulent Prandtl number, all with the a help of a quite different combination of cold and hot wires (120° X probe). Dowling and Dimotakis [9] performed measurements in a turbulent gas axisymmetric jet discharging into a different quiescent gas, using Rayleigh diffusion to yield gas concentration and give results concerning mean and fluctuating concentration fields and the concentration spectrum.

An extensive study of mass transfer in a helium jet flowing in ambient air was undertaken by Panchepakesan and Lumley [10], using an interference probe in order to obtain the helium mass fraction, combined with 2D hot wire anemometry. The distribution of the mean and fluctuating characteristics of the flow, such as multiple correlations between the helium mass fraction and the velocity components and also the turbulent kinetic energy and scalar variance budget were presented. An experimental investigation of an axisymmetric jet discharging in a co-flowing air stream has been performed by Antonia and Bilger [11]. The flow study indicates that in such a situation, self-preservation does not apply and that the far jet flow may be strongly dependent on the nozzle injection conditions.

A large part of the experimental studies referenced in the literature have been conducted in gaseous flowfields, where combined hot wire anemometry and cold wire thermometry are frequently used in order to evaluate the turbulent transport. The experimental validation of second order closure schemes for passive scalar turbulent transport in axisymmetric water jet flow is not treated in the above mentioned papers.

The present paper is devoted to the study of momentum and passive mass transport in a turbulent water jet discharging into a low velocity co-flowing stream. In the present study, a non-intrusive technique based on combined 2D laser Doppler velocimetry (LDV) and laser induced fluorescence (LIF) applied to concentration

measurements is developed. Instantaneous and simultaneous measurements in the same probe volume of two velocity components and the molecular fluorescent tracer concentration can be performed. The experimental results for the mean and fluctuating velocity and concentration fields are compared with free jet data available in literature. The effects of the co-flowing stream on the turbulent mixing process are therefore highlighted in the present study. Data for the Reynolds shear stress, turbulent longitudinal and transverse fluxes and moments involving correlations (to third order) of both concentration and velocity fields are obtained. The budgets of the governing equations of turbulent momentum and mass transport are considered and both the pressure-strain correlation and pressure scrambling terms are estimated. A second order closure model, developed by Launder [12] has been applied and validated in the light of the experimental data.

2. Flow facilities and experimental techniques

The flow facility consists of a square (side, 63 mm) test section, length 1.5 m (*figure 1*). A cylindrical nozzle (exit diameter $d = 1$ mm), fed by a pressurized reservoir of water is placed in the test section, allowing a $U_0 = 10$ ms^{-1} flow velocity at the exit. Consequently, the operating Reynolds number is $R_0 = 10000$. A low concentration of fluorescent tracer, rhodamine B ($\mathbf{C} = 5 \times 10^{-6}$ moll^{-1}), has been diluted in the water of the reservoir. The very low level of tracer concentration ensures that the physical properties of the fluid are not changed. Large optical accesses have been incorporated in the lateral wall of the test channel. A low velocity co-flowing stream ($U_1 = 0.5$ ms^{-1}) is established in the test section by means of a pump, in order to avoid pollutant accumulation rather than for fluid mechanics considerations. The flows, including the nozzle flow and ambient flow, are seeded with 30 μm diameter solid particles for the laser Doppler velocimetry measurements.

Furthermore, working with a jet in a co-flowing stream reduces errors in regions of high turbulence levels, such as at the edge of the jet, but at the expense of destroying the self-preservation properties [11]. Generally speaking, jets moving in a stream exhibit two similarity regions, one called strong jet, when the excess velocity is larger than the ambient velocity, and one like a wake, but with a positive excess velocity, when the excess velocity is much smaller than the ambient. With the present flow conditions, which are a trade-off between the flow regime and the testing loop capacities, we are able to work on the margin of the strong jet regime.

Combined laser-induced fluorescence and 2D laser Doppler velocimetry allows simultaneous and instantaneous measurements of velocity and molecular concentration of the tracer to be performed, with a frequency response compatible with the turbulence time scales. The major part of the technical details relevant to the

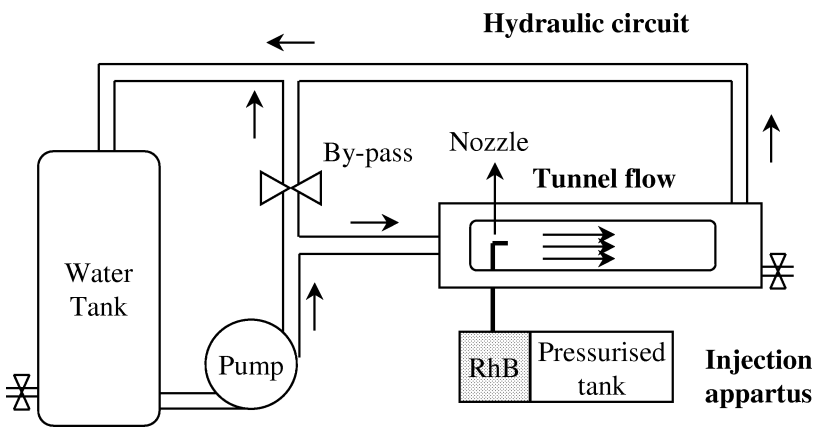

Figure 1. Schematic flow diagram.

method has been already published by Lemoine et al. [13]. The technique has been validated by an extensive study of the turbulent transport in the wake of a grid ([14,15]). The principal features of the technique are summarized here. The main component of the experimental set-up consists of a 2D laser Doppler velocimeter equipped with an argon ion laser, used in multiline mode (wavelengths $\lambda = 488$ nm and $\lambda = 514.5$ nm) in order to measure two velocity components. The selected passive contaminant is an organic dye, rhodamine B. This dye is very soluble in water, its Schmidt number is about 2740 [16] and its quantum efficiency is high, thereby providing a highly detectable red-orange fluorescence. Moreover, its fluorescence can be easily induced by the green line ($\lambda = 514.5$ nm) of the laser source of the velocimeter. If the concentration of the dye is low enough, the attenuation of the laser beam and of the fluorescence signal along their optical paths can be neglected. As a consequence, the instantaneous measured fluorescence signal turns out to be directly proportional to the molecular concentration of the tracer.

The frequency response of the fluorescence, related to the lifetime of the excited state of the molecule, is very high, exceeding more than 10^6 Hz. The concentration fluctuations due to turbulence may be then detected. The probe volume for both laser Doppler velocimetry and laser-induced fluorescence is the intersection point of three laser beams for measuring two velocity components. Considering the interference volume and the collection device, the dimensions of the measuring volume are respectively about 250 μm and 20 μm along the transverse and longitudinal directions of the flow. Two kinds of signals are emitted from the probe volume (*figure 2*). One is the Doppler signal and the other is the fluorescence of rhodamine B, emitted at higher wavelengths than the former. The same optics collect the Doppler and fluorescence signals. These optical signals are subsequently separated and processed. The first part of the optical signal is processed by two parallel channels, made up of a photomultiplier connected to a frequency tracker, in order to yield instantaneously two velocity components. The second part passes first through a high-pass filter in order to eliminate Mie scattering due to the incident laser radiation and then is detected by a second photomultiplier, to provide the fluorescence signal which is proportional to the tracer concentration. The present device allows one to measure simultaneously, instantaneously and at the same point the molecular concentration of the passive tracer, and the

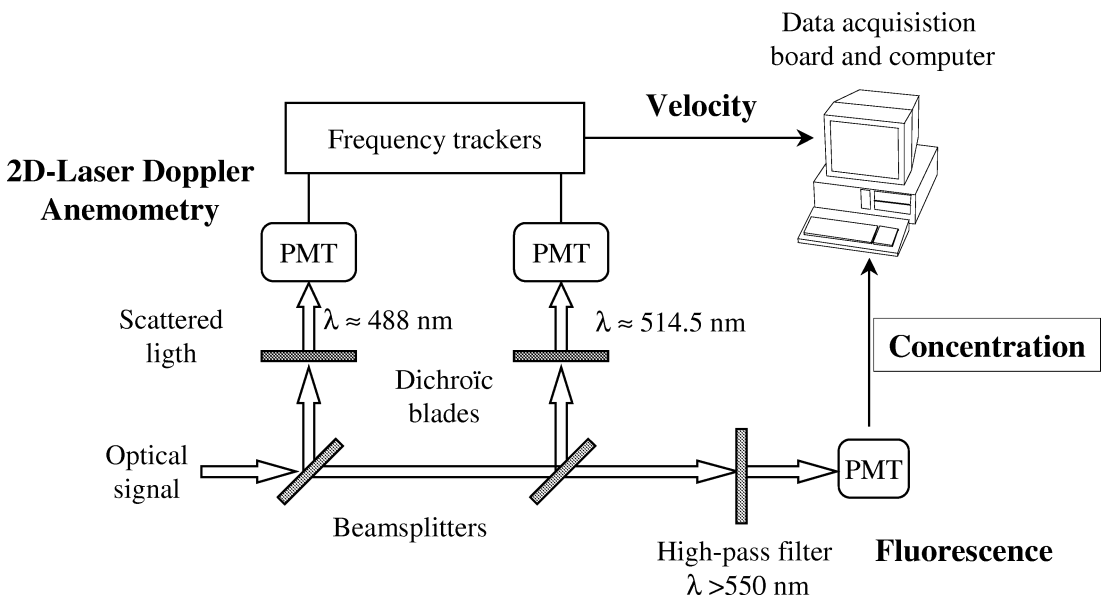

Figure 2. Optical arrangement.

velocity. The collapse of the two measuring volumes for concentration and velocity avoids the spatial bias in the calculation of the correlations involving concentration and velocity.

Data such as the analog Doppler and fluorescence signals are transmitted to a computerized acquisition board, where they are sampled and processed. One of the difficulties is that the fluorescence signal appears continuous while the LDV signal is non-continuous. However, the frequency trackers used for the Doppler signal processing give a quasi-continuous signal when the system is locked in frequency. This condition is satisfactory when the seeding rate is sufficient, in order to have at any time at least one particle in the probe volume. The acquisition of the data relevant to the LDV and fluorescence signals are synchronized to within 200 ns, which allows one to calculate cross-correlations. The sampling rate must be a trade-off between the probe volume size and the resolved turbulent structures characteristic scales. The Kolmogoroff microscale l_k in a circular jet may be estimated with the help of the relation investigated by Antonia et al. [17], as a function of the Reynolds number R_0 based on the injection velocity:

$$\frac{l_k}{d} = \left(48R_0^3\right)^{-1/4}\left(\frac{x}{d}\right). \tag{1}$$

Although this relation depends on the particular initial conditions, which are different from experiment to experiment, we have used it in the present case in order to provide a rough estimate of the characteristic scales. In the present study, measurements are performed between $x/d = 70$ and $x/d = 140$, where the variation of Kolmogoroff microscale is estimated from 27 μm to 53 μm. This scale is clearly not resolved by the probe volume of the technique, and the same is true for the Batchelor microscale for the passive scalar field, which is about 50 times smaller than Kolmogoroff microscale ($l_B = l_k/\sqrt{S_C}$). According to the same authors, the Taylor microscale can be estimated by:

$$\frac{\lambda}{d} = 0.88(R_0)^{-1/2}\left(\frac{x}{d}\right). \tag{2}$$

The Taylor microscale evolves in the investigated region of the jet from 0.6 mm to 1.232 mm, which is clearly resolved by the probe volume. The non-resolution of both Kolmogoroff and Batchelor scales can cause a statistical smoothing of the smallest fluctuations. However, the turbulent transport phenomena are governed by the large turbulent structures [7], and the conclusions about both turbulent transport of momentum and scalar budgets should therefore not be strongly affected by the limited resolution of the instruments. Considering that the resolution of the technique is given by the longitudinal size of the probe volume and that structures are convected across the probe volume at the mean longitudinal centerline velocity, the maximum frequency which can be resolved is about 5 kHz. As a consequence, the Shannon sampling rate is adjusted to 10 kHz. To ensure that adequate statistics were collected, a data acquisition record must last many times longer than the mean convection time of the local jet diameter $D(x)$. This timescale τ has been estimated from the results on the jet expansion and centerline velocity $U_m(x)$ decrease, $\tau = D(x)U_m^{-1}(x)$. The data acquisition time, fixed at 5 s, varies from about 620τ to 140τ. The sampling interval is therefore adequate in the jet centerline region, but also in the edges due to the presence of the co-flowing stream.

The accuracy of the technique has been checked: the accuracy on the concentration measurement is about 3% in term of repeatability: 1% can attributed to the non-linearity of the photodetectors and 2% to the random error due to data processing [13]. The accuracy on the velocity measurement is about 2%, according to the apparatus manufacturer.

3. Mean flow characteristics and second order moments

A first experiment allows one to characterize the injection conditions: we have observed that the longitudinal velocity profile measured close to the injection nozzle ($x/d = 0.5$) was roughly flat and the turbulence intensity in the jet core was about 4%.

The major part of the measurements of the present work has been realized in the self-preserving zone of the jet. According to Wygnanski and Fiedler [5], this zone begins at $x/d = 70$, although self-preservation is observed for the mean characteristics at about $x/d = 10$. The experimental results obtained in the present paper will be compared with other authors' data referenced in *table I* where experimental parameters and flow parameters are summarized.

The present jet is described using the cylindrical coordinates system (r, θ, x) indicating the radial, azimuthal and longitudinal directions of the flowfield. All the measured parameters will be normalized by the local centerline value of longitudinal velocity or concentration, and the radial distance r by the axial location x, r/x. The main notations are presented in *figure 3*.

3.1. Dynamic field

The streamwise distribution of the centerline longitudinal velocity relative to the velocity of the co-flowing stream is reported in *figure 4* and is in agreement with the results of [4,6,18,19] plotted in the same figure. The streamwise velocity decay can be written as a hyperbolic law:

$$\frac{\overline{U}_0}{\overline{U}_m} = \frac{1}{K}\left(\frac{x - x_0}{d}\right), \tag{3}$$

where $K = 6.83$ and the virtual origin x_0 is $4.9d$; $\overline{U}_0$ is the injection velocity and $\overline{U}_m$ the local centerline excess velocity. Despite the presence of the co-flowing stream, the decay rate of the centerline velocity is in reasonable agreement with other authors' values, such as those reported in [4,18], shown in *table II*. The excess velocity above the co-flow velocity is about 1.1 ms^{-1} at $x/d = 70$ and 0.5 ms^{-1} at $x/d = 140$. Indeed, the effect of

Table I. Flow parameters for various studies of the axisymmetric turbulent jet.

Authors	Operating Reynolds number	Fluid	Passive contaminant	Diagnostic
Hinze and Van der Hegge Zijnen [4]	6.7×10^4	air/gas	Temperature/Concentration	Pitot tube, Cr-Al thermocouple Total-head tube
Becker et al. [20]	5.4×10^4	air	Oil fog/Concentration	Light diffusion
Wygnanski and Fiedler [5]	10^5	air		Hot wires
Chevray and Tutu [7]		air	Temperature	Hot and cold wires
Papanicolaou and List [19]	1.1×10^4	water	Rhodamine 6G/Concentration (Fluorescent dye)	Laser Doppler anemometry Laser induced fluorescence
Chua and Antonia [8]	1.7×10^4	air	Temperature	Hot and cold wires
Dowling and Dimotakis [9]	5×10^3 to 4×10^4	air	Gas/Concentration	Rayleigh diffusion
Panchapakesan and Lumley [18]	1.1×10^4	air		Hot wires
Panchapakesan and Lumley [10]	1.1×10^4	air	Helium/Concentration	Hot wires and interference probes
Hussein et al. [6]	9.55×10^4	air		Flying hot wires and LDA
Present study	1.05×10^4	water	Rhodamine B/Concentration (fluorescent dye)	Laser Doppler anemometry Laser induced fluorescence

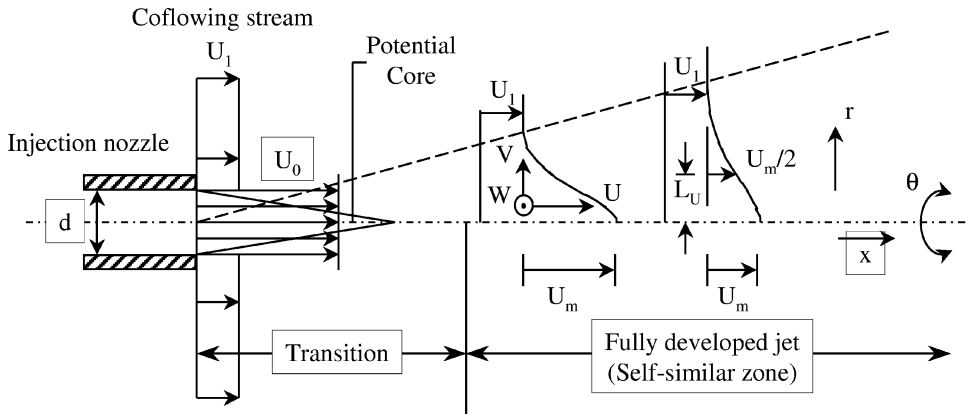

Figure 3. Sketch of the axi-symmetric jet and notations.

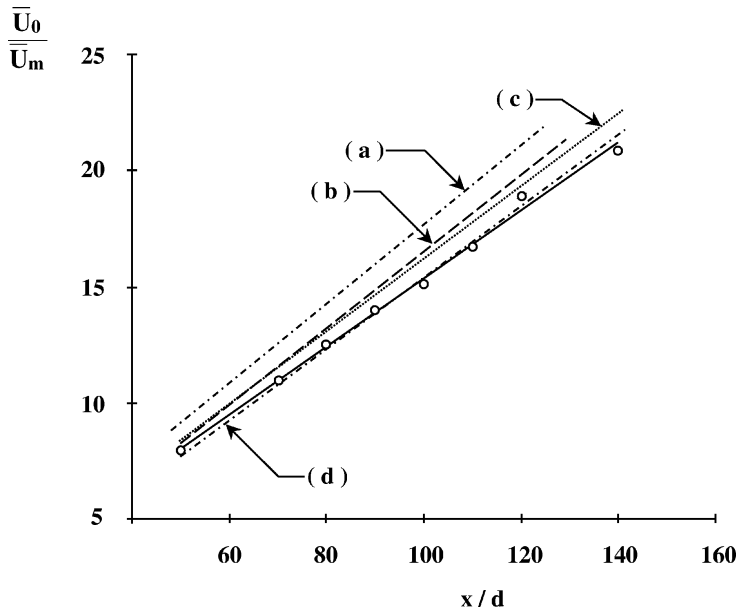

Figure 4. Streamwise variation of centreline mean longitudinal velocity $\overline{U}_0/\overline{U}_m$: ∘ present; (a) [6]; (b) [18]; (c) [4] and (d) [19].

the co-flow on the jet can be estimated from the results of Reichardt (in [9]) , who defined the momentum lengthscale l_c associated with a jet in a co-flowing stream:

$$l_c^2 = \frac{4}{\pi U_1^2} \int_{A_0} (U_0 - U_1) U_0 \, \mathrm{d}A, \tag{4}$$

where A_0 refers to the jet nozzle area and U_1 to the co-flow velocity. Reichardt's work shows that the co-flowing stream influence on the jet begins to be noticeable for $x/l_c > 1$. For the present conditions, $l_c \approx 40$ mm, which means that the co-flow should influence the jet from $x/d = 40$, and particularly in the measurement zone. The results of the present study will be compared with other free jet works and the differences will be highlighted.

The radial distributions of the longitudinal velocity $\overline{U}$ (*figure 5*) appears self-similar and appears to be Gaussian, in agreement with other authors' data such as [5,18]. The spreading rate of the jet, determined

Table II. Measured parameters for various studies of the axisymmetric jet referenced in the literature.

Authors		[4]	[20]	[5]	[19]	[9]	[18]	[10]	[6] (HW)	[6] (LDA)	Present
Measurements range		$\frac{x}{d} < 140$	$\frac{x}{d} < 45$	$\frac{x}{d} < 100$	$\frac{x}{d} < 120$	$\frac{x}{d} < 80$	$\frac{x}{d} < 150$	$\frac{x}{d} < 120$	$\frac{x}{d} < 120$	$\frac{x}{d} < 120$	$\frac{x}{d} < 140$
Axial decays	K	6.39	10.8	$\frac{5.3^{(*)}}{4.7^{(**)}}$	6.71	×	6.06		5.8	5.9	6.83
	$K^{(S)}$	5.27	×	×	6.33	5.11	×	2.41	×	×	6.76
Virtual origins	x_0	$0.6d$	$2.4d$	$\frac{3d^{(*)}}{7d^{(**)}}$	$2.56d$		0		$4d$	$2.7d$	$4.9d$
	$x_0{}^{(S)}$	$0.8d$			$6d$	$-3.7d$		0			$-11d$
Velocity profile expansion coefficient		0.0827	0.106	0.086	0.104		0.116		0.094	0.102	0.064
Scalar profile expansion coefficient		0.0965			0.139	0.105		0.138			0.074
ratio r_C/r_U		1.16			1.33			1.19			1.15

Measurements for $^{(*)}$ $x/d < 50$ and $^{(**)}$ $x/d > 50$

$^{(S)}$ Measurements concerning the scalar (Concentration / temperature)

HW: Hot wire measurements

LDA: Laser Doppler anemometry measurements

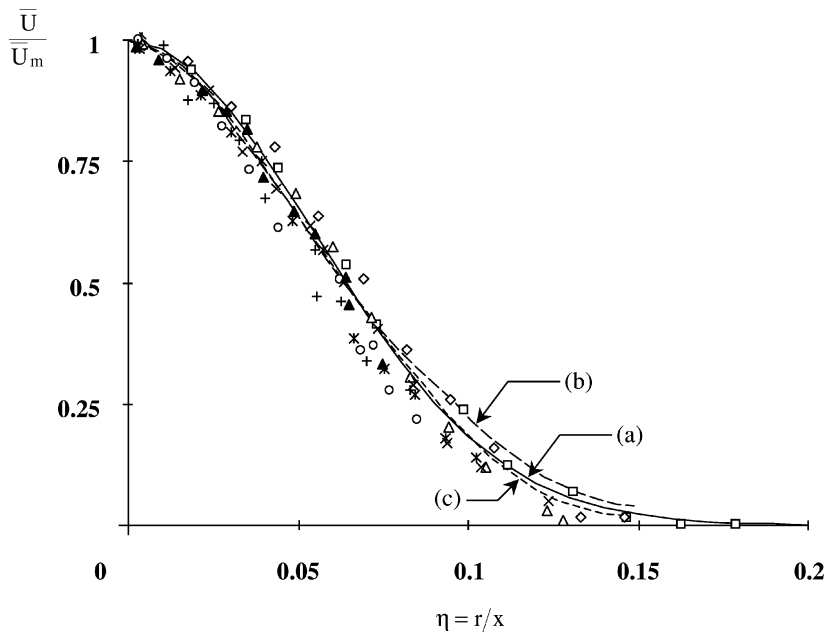

Figure 5. Longitudinal mean velocity profiles: □ $x/d = 50$; ◇ $x/d = 70$; △ $x/d = 80$; × $x/d = 90$; ∗ $x/d = 100$; ○ $x/d = 110$; + $x/d = 120$; ▲ $x/d = 140$; (a) fit of present measurements; (b) [5] and (c) [18].

with the help of the streamwise evolution of the half-width radius L_u of the longitudinal velocity profile is $L_u/d = 0.064x/d$. This value is about 30% less than those determined by other authors in a free jets (see also *table II*). This low value of the spreading rate can be attributed mainly to the presence of the co-flowing stream, tending to reduce the jet expansion. The effect of the side walls of the enclosure can be excluded here, since the half-width jet diameter is about 18 mm, whereas the enclosure dimension is 63 mm, which can be compared to the operating conditions of Antonia and Bilger [11], where no side walls effects were noticed. Furthermore, it has been checked that the velocity profile remains axisymmetric, even at $x/d = 140$. Nevertheless, the present

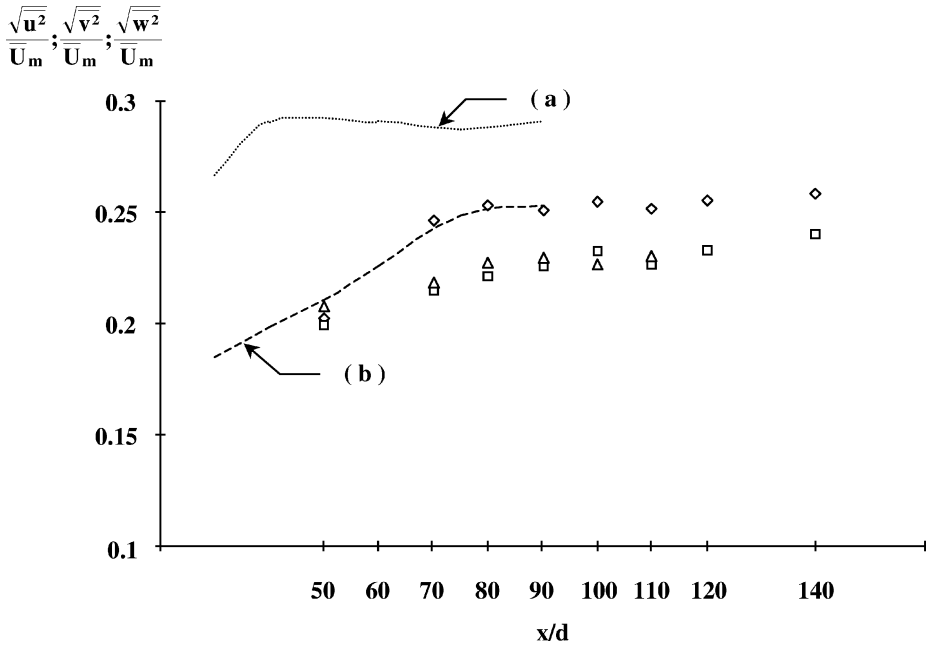

Figure 6. Variation of turbulent intensities along the jet centreline. Present: ◇ $\sqrt{\overline{u^2}}/\overline{U_m}$; □ $\sqrt{\overline{v^2}}/\overline{U}_m$; △ $\sqrt{\overline{w^2}}/\overline{U}_m$, [5]: (a) u component; (b) v component.

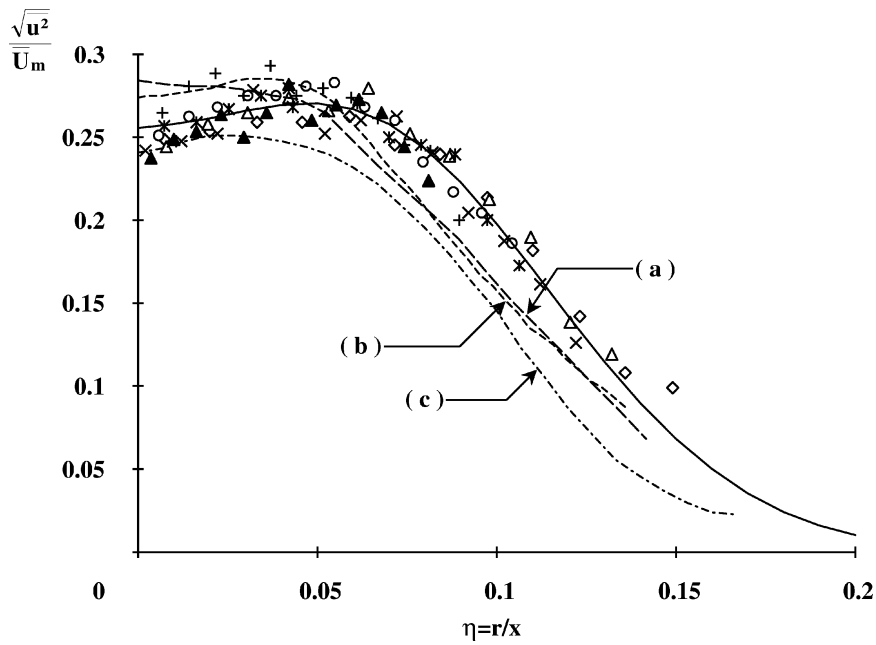

Figure 7. Axial turbulent intensities $\sqrt{\overline{u^2}}/\overline{U}_m$ across the jet. Present: ◇ $x/d = 70$; △ $x/d = 80$; × $x/d = 90$; ∗ $x/d = 100$; ○ $x/d = 110$; + $x/d = 120$; ▲ $x/d = 140$; — fit of present and: (a) [5]; (b) [6] (LDA); (c) [18].

measurements have been compared with the results of other authors by determining the radial dimensionless coordinate on the basis of similar spreading rates. *Table II* gives a list of the various studies referenced in this paper and the spreading rates which will be used to compare the radial scales.

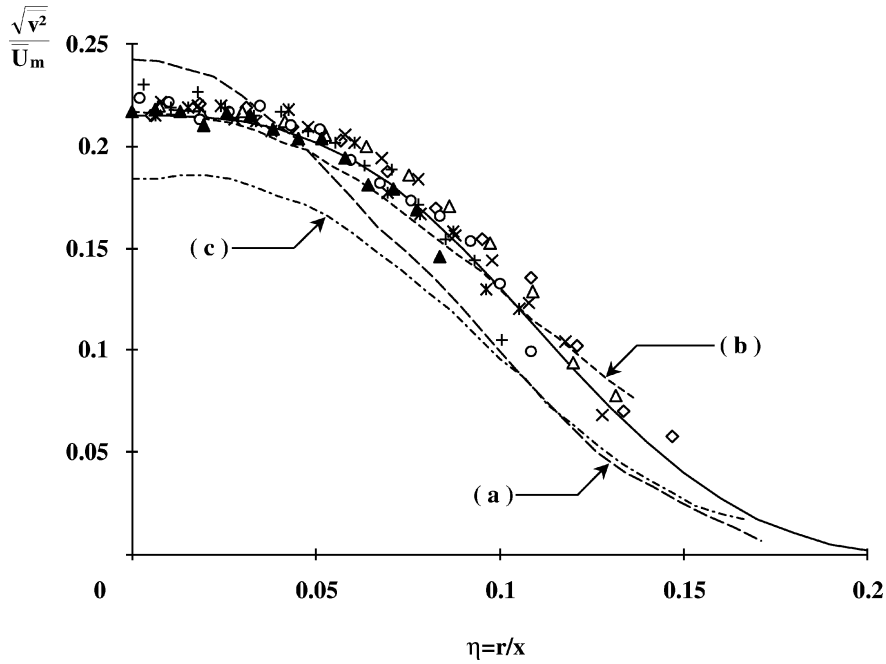

Figure 8. Radial turbulence intensities $\sqrt{\overline{u^2}}/\overline{U}_m$ across the jet. (See *figure 7* for symbols.)

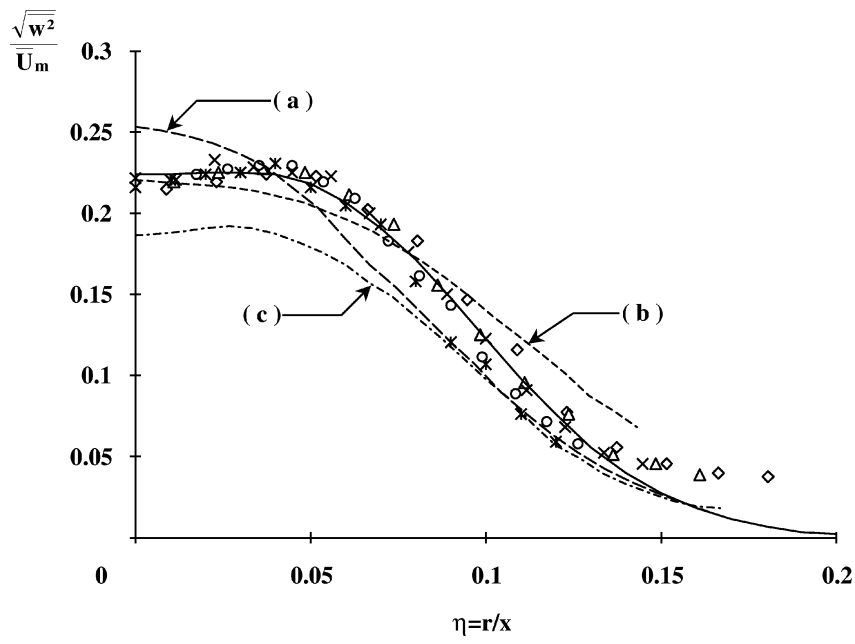

Figure 9. Azimuthal velocity turbulence intensities $\sqrt{\overline{w^2}}/\overline{U}_m$ across the jet. (See *figure 7* for symbols.)

In the light of the streamwise distribution of the second order moments of the velocity components fluctuations $\overline{u^2}$, $\overline{v^2}$ and $\overline{w}^2$ on the jet centerline (*figure 6*), it appears that the magnitude of $\overline{u^2}$ is everywhere greater than $\overline{v^2}$ and $\overline{w}^2$, which agrees well with the results of [5] reported on the same figure, in spite of the significant differences in the measured values. The kinetic energy is first transferred from the mean motion to the longitudinal component of the fluctuating velocity u and is redistributed to the other fluctuating components v and w by pressure fluctuations. The longitudinal velocity fluctuations first becomes self-similar for distances from nozzle exit higher than $x/d = 70$ (*figures 6* and *7*) while the azimuthal and radial fluctuations reached self-similarity from $x/d = 90$ to $x/d = 100$ (*figure 6*). It can be also noted that the intensity of turbulence in the radial and azimuthal directions (*figures 8* and *9*) have the same order of magnitude: intensity of turbulence is of the order of 0.2 to 0.22 for v and w as it is 0.25 for u. An off-axis peak can be observed in the longitudinal fluctuating component but not on the other. Despite the radial expansion reduction, the present measurements are in good agreement with the experimental data reported in [6] obtained on a free jet by laser Doppler anemometry, and are higher than measurements reported in [18]. Some differences with the results of [5], in relation to the centerline value, can also be observed.

3.2. Scalar field

The streamwise decay of the mean fluorescent tracer concentration $\overline{C}_m$ is presented in *figure 10* and follows an usual hyperbolic law:

$$\frac{\overline{C}_0}{\overline{C}_m} = \frac{1}{K^{(S)}}\left(\frac{x - x_0^{(S)}}{d}\right), \tag{5}$$

where $K^{(S)} = 6.76$ and the virtual origin $x_0^{(S)}$ is $-11d$ and $\overline{C}_0$ is the injection concentration.

The constant $K^{(S)}$ is comparable to those measured by [19], with a Schmidt number of about 700, and a large scatter in the virtual origin between different works, can be observed (see *table II*). The normalized radial

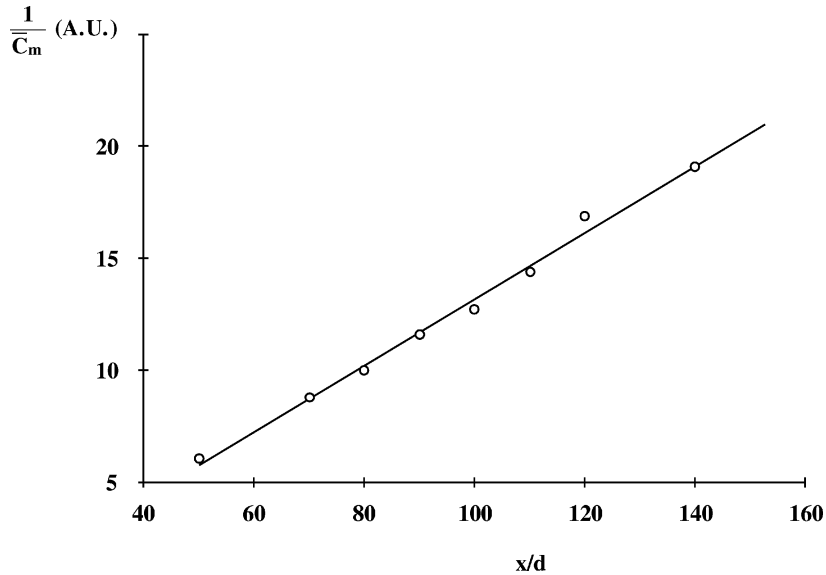

Figure 10. Streamwise variation of centreline mean concentration $1/\overline{C}_m$: — fit of the present measurements. (Measurements are presented in Arbitrary Units.)

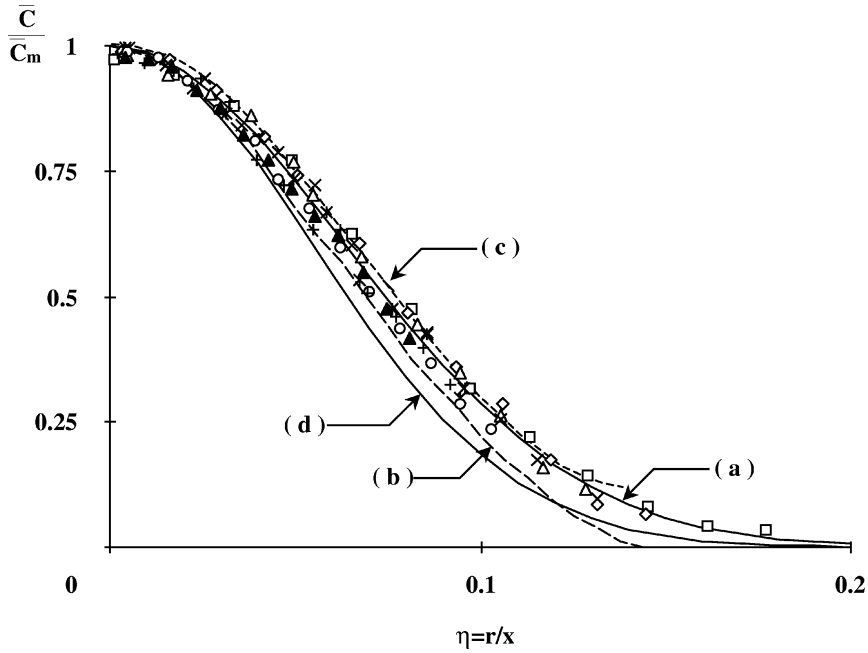

Figure 11. Distribution of mean concentration across the jet. Present: □ $x/d = 50$; ◇ $x/d = 70$; △ $x/d = 80$; × $x/d = 90$; ∗ $x/d = 100$; ∘ $x/d = 110$; + $x/d = 120$; ▲ $x/d = 140$: (a) fit of present measurements; (b) [9] and (c) [10]. Comparison to the mean longitudinal velocity profile (d).

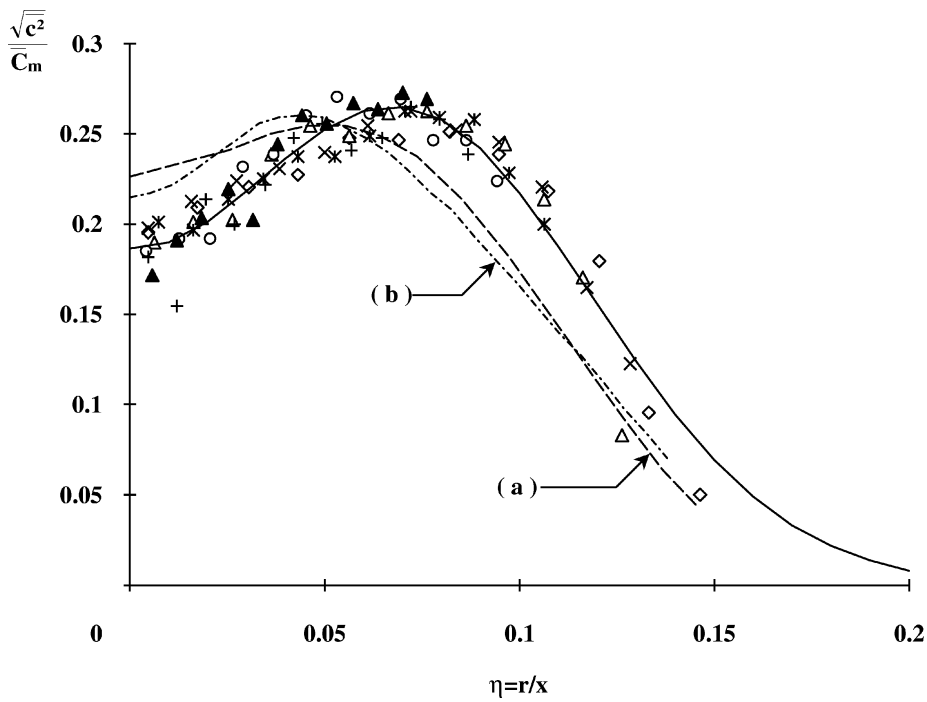

Figure 12. Distribution of turbulence intensity of concentration fluctuations $\sqrt{\overline{c^2}}/\overline{C}_m$. Present: ◇ $x/d = 70$; △ $x/d = 80$; × $x/d = 90$; ∗ $x/d = 100$; ∘ $x/d = 110$; + $x/d = 120$; ▲ $x/d = 140$; —— fit of present; (a) Becker et al. [20] and (b) [10].

concentration profiles are reported *figure 11*, in comparison with the self-similar velocity profiles. As for the velocity profiles, the mean concentration profiles appear self-similar and Gaussian-like from $x/d = 50$ and present a Gaussian aspect. This distribution agrees very well with [10] results. However, the profiles reported by Dowling and Demotakis [9], obtained for a Schmidt number of the order of 1, appear narrower.

The flatter distribution of concentration in comparison to the velocity can be interpreted by the fact that the scalar is transported by the velocity vector and not only by its longitudinal component. Furthermore, it can be added that the high value of the Schmidt number ensures that the momentum diffuses faster than the scalar.

The spreading rate of the scalar field, determined by means of streamwise evolution of the half-width radius L_c of the concentration profiles is $L_c/d = 0.074x/d$. This is clearly, as in the case of the longitudinal velocity, lower than other authors' results. However, the scalar to momentum spreading rate ratio is about 1.15, which is in full agreement with previous results obtained in the free jet, summarized in *table II*.

The distribution of the fluctuating concentration across the jet is shown in *figure 12*, normalized by the centerline value of the mean concentration, and compared with other experiments referenced in the literature. As in the other authors' works (e.g. [10] or Becker et al. [20]), the fluctuating concentration presents an off-axis peak.

In the light of the previous studies relevant to mean and second order moments of velocity and concentration fields, the experimental results are similar to the results available for free jets and self-preservation properties are checked. A lower spreading rate is to be expected since the rate of spread is known to be very sensitive to the excess velocity ratio. This is an important parameter to take into account when comparing results from different studies.

4. Turbulent momentum and mass transport

4.1. Governing equations

The general equations governing momentum and mass transport in the jet are presented in this section under the following hypothesis: the flowfield is statistically stationary and axisymmetric. All the equations are written in the cylindrical coordinates system (r, θ, x) and all derivates with respect to the angular position θ will be equal to zero ($\partial/\partial\theta = 0$). The azimuthal mean component of velocity is zero ($\overline{W} = 0$) since there is no swirl and all correlations involving odd powers of the azimuthal velocity fluctuations will be also zero. Finally, equations are considered under the boundary layer approximation.

Under the above mentioned hypothesis, the transport equation of the Reynolds shear stress $\overline{uv}$ may be written by neglecting molecular diffusion and turbulent diffusion by pressure fluctuations and using local isotropy hypothesis for dissipation, such that:

$$\overbrace{\overline{V}\frac{\partial\overline{uv}}{\partial r} + \overline{U}\frac{\partial\overline{uv}}{\partial x}}^{\text{Advection (I)}} = \underbrace{-\overline{v^2}\frac{\partial\overline{U}}{\partial r}}_{\text{Production (II)}} + \overbrace{\overline{\frac{p}{\rho}\left(\frac{\partial u}{\partial r} + \frac{\partial v}{\partial x}\right)}}^{\text{Pressure-strain correlation (III)}} \underbrace{- \frac{\partial\overline{uv^2}}{\partial r} - \frac{\overline{uv^2}}{r} + \frac{\overline{uw^2}}{r}}_{\text{Diffusion (IV)}}. \tag{6}$$

Neglecting molecular diffusion and turbulent diffusion by pressure fluctuations, the scalar transport problem is governed by the turbulent flux $\overline{vc}$ equation, which may be written:

$$\overbrace{\overline{V}\frac{\partial\overline{vc}}{\partial r}+\overline{U}\frac{\partial\overline{vc}}{\partial x}}^{\text{Advection (I)}}=\underbrace{-\overline{v^2}\frac{\partial\overline{C}}{\partial r}-\overline{vc}\frac{\partial\overline{V}}{\partial r}}_{\text{Production (II)}}-\overbrace{\frac{1}{\rho}\overline{c\frac{\partial p}{\partial r}}}^{\text{Pressure-scrambling (III)}}\underbrace{-\frac{\partial\overline{v^2c}}{\partial r}-\frac{\overline{v^2c}}{r}+\frac{\overline{w^2c}}{r}}_{\text{Diffusion (IV)}}. \tag{7}$$

The majority of the terms in both the Reynolds shear stress and the turbulent flux transport equations can be determined experimentally, except the pressure-strain correlation and the pressure scrambling terms. The radial velocity distribution can be obtained by the resolution of the continuity equation. A budget on both equations allows us to determine the unknown terms.

4.2. Reynolds shear stress transport

The radial distribution of the Reynolds shear stress $\overline{uv}$ is presented in *figure 13*, using normalized values. Except the spreading rate of the jet, the results are in agreement with measurements of [6,18] but the profile reported in [5] seems to be narrower and presents a lower magnitude. The maximum of shear stress, is located at $\eta = 0.055$, close to the maximum mean shear stress. A small shift in the maximum position can be observed in comparison with data reported in the literature. It can be observed that the co-flowing stream effect seems not to influence severely the momentum turbulent transport process. This fact is confirmed by calculating the distribution of $\overline{uv}/\overline{U}_m^2$ (also reported in *figure 13*) inferred from the momentum equations and the measured mean velocity profile and considering formal self-similarity assumptions [8]. Although the calculation and the

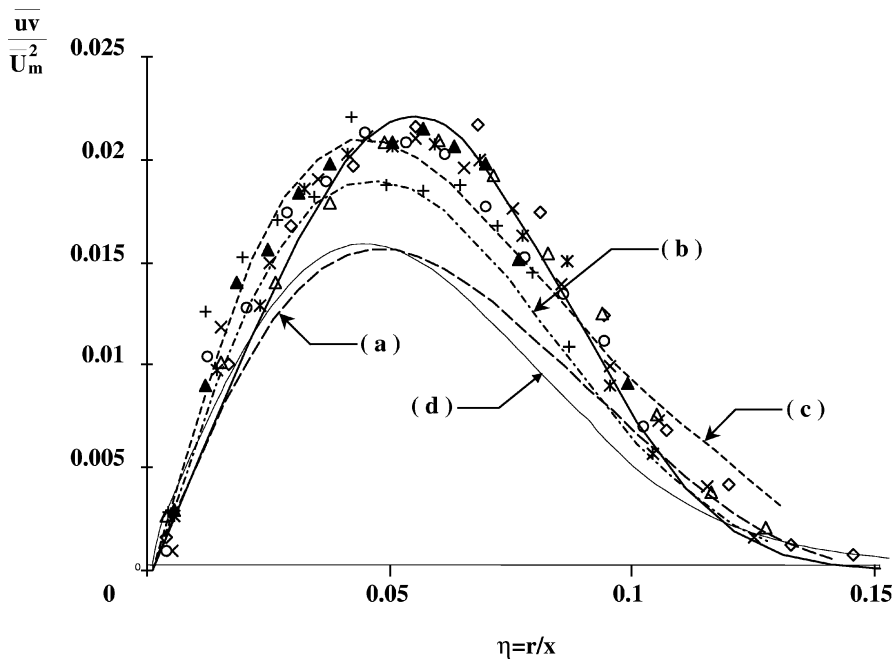

Figure 13. Distribution of Reynolds shear stress $\overline{uv}/\overline{U}_m^2$ across the jet: (a) [5]; (b) [18] and (c) [6] (LDA); (d) calculation; —— fit of the present measurements. (See *figure 7* for symbols.)

measurements present similar shapes, a significant difference, up to 30% can be observed. It can be attributed to the lack of formal self-similarity in presence of a co-flowing stream, previously highlighted by Antonia and Bilger [11].

4.2.1. Higher moments

The triple correlation radial profiles $\overline{uv^2}$ and $\overline{uw^2}$ have also been measured. The data are not shown here, but a complete data set can be obtained from the authors. The distribution and orders of magnitude of both triple correlations appear similar and hence self-similarity is also checked in the investigated region. In the jet center region, the correlations $\overline{uv^2}$ and $\overline{uw^2}$ appear negative as in the results of [6] or [18], even though measurements reported by these authors are higher. The present data differ significantly from the results in [5], where no negative zones were found. The maximum value of both triple correlations $\overline{uv^2}$ and $\overline{uw^2}$ is reached at $\eta = 0.075$ and the sign changes at $\eta = 0.035$.

4.2.2. Budget for the Reynolds shear stress

The budget for the Reynolds shear stress transport equation has been calculated and is shown in *figure 14*. All the terms of the budget have been normalized by $L_u/\overline{U}_m^3$ where $L_u = r_u \cdot x$ is a characteristic length scale of the flowfield. The longitudinal and radial gradients have been calculated from the self similar profiles in the following way and using equation (3):

$$\frac{Q^p}{\overline{U}_m^p} = f(\eta); \qquad \frac{L_u}{\overline{U}_m^p}\frac{\partial Q^p}{\partial r} = r_u \frac{\mathrm{d}f(\eta)}{\mathrm{d}\eta}; \qquad \frac{L_u}{\overline{U}_m^p}\frac{\partial Q^p}{\partial x} = -r_u\left(pf(\eta) + \eta\frac{\mathrm{d}f(\eta)}{\mathrm{d}\eta}\right), \tag{8}$$

where Q^p is the p-order moment of the fluctuating velocity and $f(\eta)$ the analytical expression of the self-similar profile. Fits of the experimental data have been used in order to calculate the gradients and therefore to obtain smooth curves. As seen in *figure 14*, Reynolds shear stress production due to velocity gradients is counterbalanced by energy redistribution by pressure fluctuations, in relation to the pressure-strain correlation

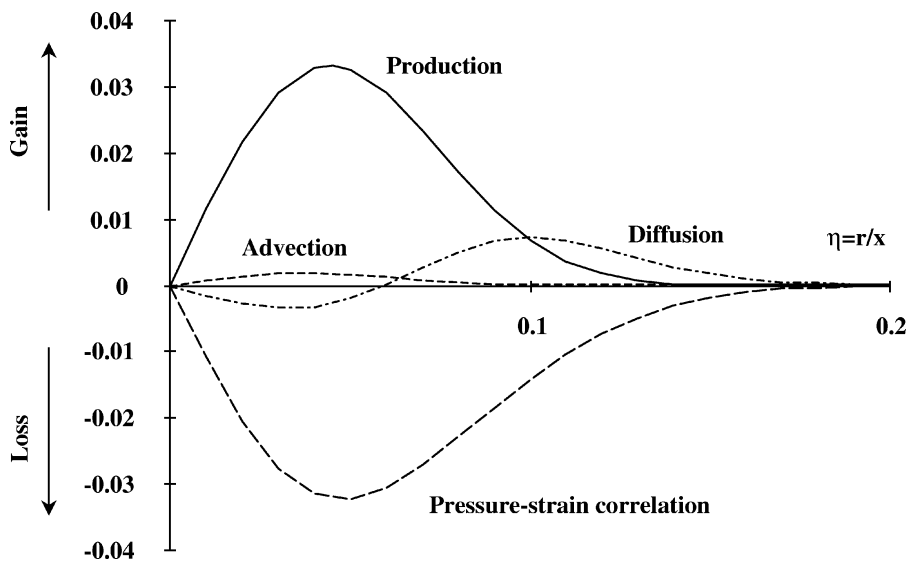

Figure 14. Budget for Reynolds shear stress transport equation in normalized values. Production: $-\overline{v^2}\partial\overline{U}/\partial r$, diffusion: $-\overline{uv^2}/r - \partial\overline{uv^2}/\partial r + \overline{uw^2}/r$ and advection terms: $\overline{V}\partial\overline{uv}/\partial r + \overline{U}\partial\overline{uv}/\partial x$. The pressure strain-correlation term: $\overline{p/\rho(\partial u/\partial r + \partial v/\partial x)}$ is deduced from the other terms.

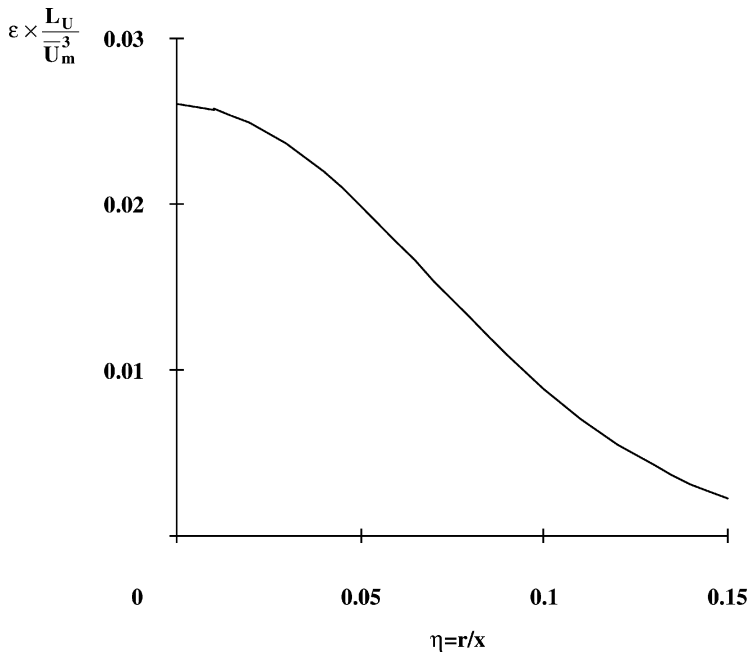

Figure 15. Normalized dissipation rate of kinetic turbulent energy $\varepsilon \times L_U/\overline{U}_m^3$ from Hussein and George [21].

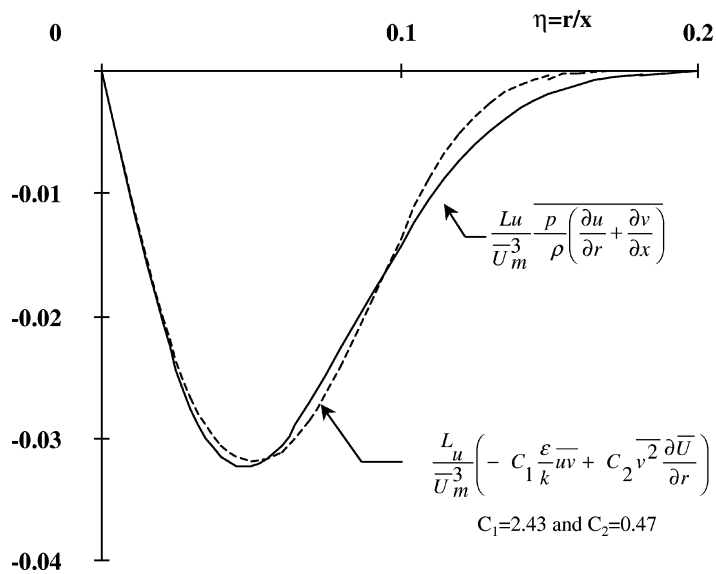

Figure 16. Closure model for the pressure-strain correlation: —— pressure-strain correlation term, and - - - - closure model. Adjustment of the two numerical constants C_1 and C_2 using least-squares fit.

term in equation (6). In the majority of the flowfield, the previously mentioned mechanisms are predominant, in comparison to advection and turbulent diffusion due to velocity fluctuations. The maximum production, which also corresponds to the maximum pressure-strain correlation, is located at $\eta = 0.05$.

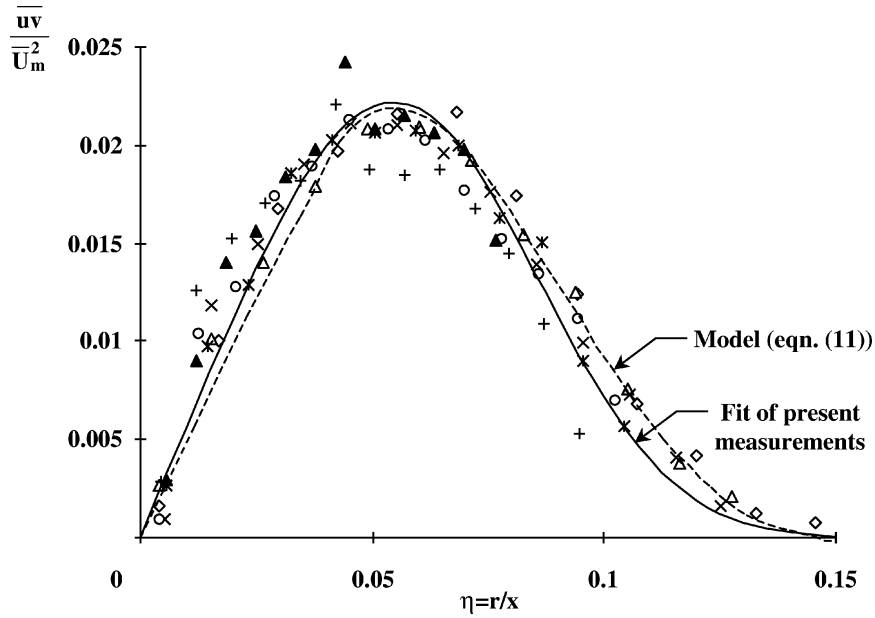

Figure 17. Model for the Reynolds shear stress (equation (11)), and comparison to the measurements: ◇ $x/d = 70$; △ $x/d = 80$; × $x/d = 90$; ∗ $x/d = 100$; ○ $x/d = 110$; + $x/d = 120$; ▲ $x/d = 140$.

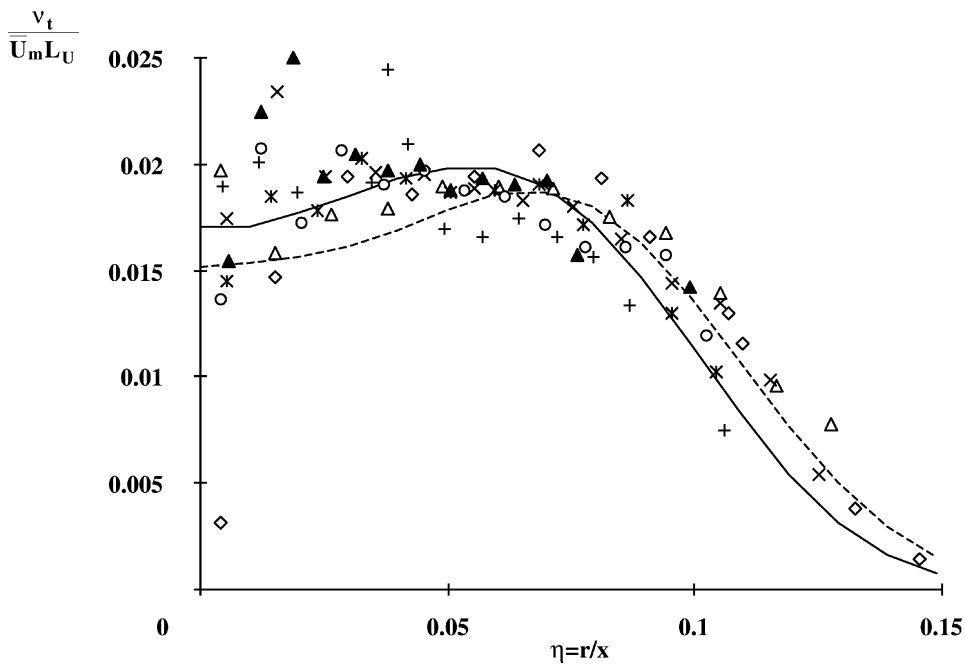

Figure 18. Distribution of the turbulent viscosity ν_t across the jet and comparison with: - - - - turbulent diffusivity model (equation (11)), $\nu_t = -\overline{uv}/\frac{\partial \overline{U}}{\partial r}$; ◇ $x/d = 70$; △ $x/d = 80$; × $x/d = 90$; ∗ $x/d = 100$; ○ $x/d = 110$; + $x/d = 120$; ▲ $x/d = 140$; —— fit of the present measurements.

According to Launder [12], and keeping boundary layer approximation in mind, the pressure strain correlation can be approximated by:

$$\overline{\frac{p}{\rho}\left(\frac{\partial u}{\partial r}+\frac{\partial v}{\partial x}\right)}=-C_1\frac{\varepsilon}{k}\overline{uv}+C_2\overline{v^2}\frac{\partial\overline{U}}{\partial r} \tag{9}$$

such that C_1 and C_2 are two numerical constants, k is the kinetic energy of turbulence and ε its dissipation rate.

It has been clearly demonstrated that the approximation pressure-strain correlation $\approx$ production is valid over the majority of the self-similar flowfield, which may be written as:

$$\overline{\frac{p}{\rho}\left(\frac{\partial u}{\partial r}+\frac{\partial v}{\partial x}\right)}=\overline{v^2}\frac{\partial\overline{U}}{\partial r}. \tag{10}$$

According to equations (9) and (10), the Reynolds shear stress may be written with the use of $\overline{v^2}$, k and ε as a variable turbulent viscosity model, defined by:

$$\overline{uv}=-\frac{k}{\varepsilon}\Phi\overline{v^2}\frac{\partial\overline{U}}{\partial r}, \tag{11}$$

where $\Phi=(1-C_2)/C_1$ is a numerical constant.

With the present measurements, the constants C_1 and C_2 can be evaluated: the kinetic energy of turbulence $k=\frac{1}{2}\overline{u_iu_i}$ is obtained from the previous measurements; the kinetic energy dissipation rate has not been measured but the measurements of Hussein and George [21] performed in a round turbulent jet, where dissipation estimated from direct derivative measurements have been used and reported in non-dimensional values, as seen in *figure 15*. The data of Hussein and George [21] have been collected at a Reynolds number of 9.5×10^5, clearly different to the present one (10^4). However, this difficulty can be overcome by the use of non-dimensional values in the self-preserving zone. Indeed, non-dimensional kinetic energy dissipation rates determined at quite different Reynolds numbers are compared in [18] and exhibit similar orders of magnitude.

The two numerical constants C_1 and C_2 are adjusted using a least-squares fit (*figure 16*) of the pressure-strain correlation term obtained from the budget of the Reynolds shear stress equation. We determined that $C_1=2.43$ and $C_2=0.47$ and the resulting value of Φ is 0.22, which is very closed to the value $\Phi=0.2$ proposed by Launder [12] with the data of homogeneous sheared turbulence in the Champagne et al. [22] experiments.

As seen in *figure 17*, the agreement between the Reynolds shear stress calculated using the numerical constants C_1 and C_2 and the present measurements was found to be very good. The distribution of turbulent momentum diffusivity $\nu_t=\frac{k}{\varepsilon}\Phi\overline{v^2}$ (turbulent viscosity) across the jet is shown in *figure 18*, in non-dimensional values ($\nu_t/\overline{U}_mL_u$) in comparison to those determined experimentally ($\nu_t=-\overline{uv}/\frac{\partial\overline{U}}{\partial r}$). The non-dimensional turbulent viscosity presents a weak evolution in the central region of the jet, thus attaining a maximum at $\eta=0.065$ and decreasing strongly in the mixing layer of the jet. The value of $\nu_t/\overline{U}_mL_u$ averaged in the jet center zone, determined from the present measurements (about 0.02), is also approximately the same as those reported by Chua and Antonia [8], where $\nu_t/\overline{U}_mL_u=0.025$ has been measured.

4.3. Scalar turbulent transport

4.3.1. Turbulent flux

The simultaneous determination of instantaneous velocity and molecular tracer concentration allows the turbulent longitudinal and radial mass fluxes $\overline{uc}$ and $\overline{vc}$ to be determined. The longitudinal turbulent flux is

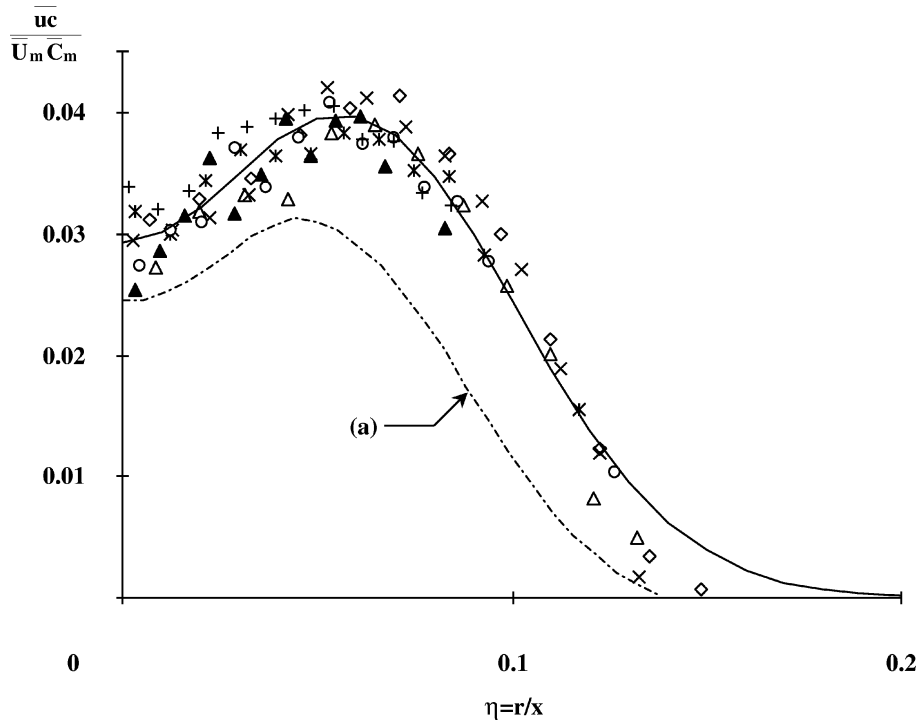

Figure 19. Distribution of the longitudinal turbulent scalar flux $\overline{uc}/\overline{U}_m\overline{C}_m$ across the jet. Present: $\diamond$ $x/d = 70$; $\triangle$ $x/d = 80$; $\times$ $x/d = 90$; $*$ $x/d = 100$; $\circ$ $x/d = 110$; $+$ $x/d = 120$; $\blacktriangle$ $x/d = 140$; —— fit of present and (a) [10].

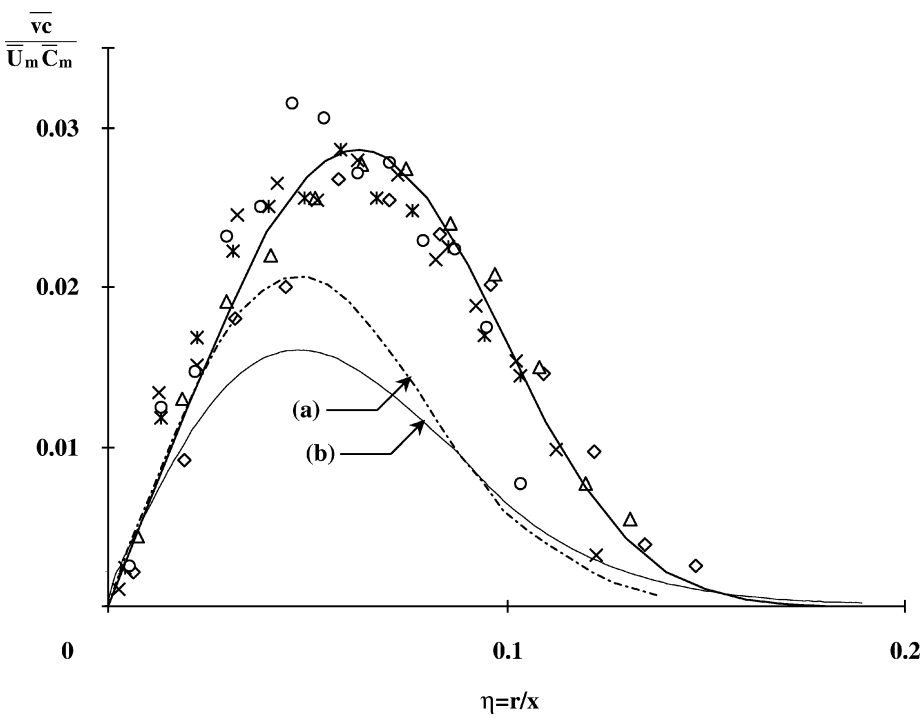

Figure 20. Distribution of the radial turbulent scalar flux $\overline{vc}/\overline{U}_m\overline{C}_m$ across the jet. (b) Calculation. (See *figure 19* for the other symbols.)

shown in *figure 19*. As expected, the longitudinal turbulent flux presents a symmetric shape and appears to be self-similar, with an off-axis maximum located at $\eta = 0.055$. The maximum corresponds to the mixing layer of the jet where the Reynolds shear stresses also reaches a maximum (see *figure 13*). The present measurements are clearly higher than the experimental data reported in [10,19] (not shown in *figure 19*). The measured maximum value is about 0.04 while the values in [10] and [19] are 0.029 and 0.021 respectfully. The radial turbulent flux $\overline{vc}$, shown in *figure 20*, does not show any deviation from the self-similar profile. The profile is antisymmetric and the extreme value is located at $\eta = 0.063$. The amplitude of the measurements appears also higher, as for the correlation $\overline{uc}$, than results reported in [10] in the self-similar zone and Chevray and Tutu [7] in the near field of the jet ($x/d = 15$), or Chua and Antonia [8], from $x/d = 15$ to 35. The maximum value is presently 0.03; other authors' values are 0.02 in [10], 0.019 for Chua and Antonia [8] and 0.015 for Chevray and Tutu [7]. A moderate shift relevant to the extreme value location should also be noted. Although self-similarity properties are observed, the magnitude of the turbulent fluxes $\overline{uc}$ and $\overline{vc}$ are clearly higher than the results available in the literature. The results of [10] are obtained in a Helium jet discharging in an air jet, so that buoyancy forces are involved in such a flowfield. However, their effects on the correlation $\overline{vc}$ appear rather low, since the results of [10] are similar with those of Chua and Antonia [8], although obtained in a different zone of the jet (from $x/d = 15$ to 35). It can be assumed that the turbulent mixing process between the clear water of the co-flow and the contaminated turbulent jet is largely enhanced by the presence of the co-flow, resulting in a higher values of the measured turbulent fluxes $\overline{uc}$ and $\overline{vc}$. This can also explain partially the important difference of the measurements with the calculation of $\overline{vc}/\overline{U}_m\overline{C}_m$ (also reported in *figure 20*) inferred from the concentration equation and the measured mean concentration profile [8]. This difference be also attributed, as well as in the case of the Reynolds shear stress, to the absence of formal self-similarity in a jet in a co-flowing stream.

4.3.2. Higher moments

The scalar triple moments present in the diffusion term of the turbulent flux transport equation have been measured. These data are not shown here, but a complete data set is available from the authors. Both cross-correlations $\overline{v^2c}$ and $\overline{w^2c}$ exhibit self-similar shapes and the same order of magnitude. The profiles are symmetric; the minimum value is located on the jet centerline ($\eta = 0$) and the maximum at $\eta = 0.085$. The results agrees qualitatively with data in [10], both show a negative region with similar zero-crossing point. However, the disagreement between the amplitudes, which can be attributed to the co-flow mixing effect, also observed on the turbulent flux $\overline{vc}$, can reach 50%.

Although there is qualitative agreement of the results with the literature on free jets, the quantitative differences remain difficult to interpret, in the light of the different operating Schmidt numbers and the different measurement techniques used.

4.3.3. Budget for scalar turbulent transport

All the terms of equation (7) can be measured with the exception of the pressure scrambling term $(-\frac{1}{\rho}\overline{c\frac{\partial p}{\partial r}})$ which can be inferred from the other terms. The budget for scalar turbulent transport equation, normalized by $L_u/\overline{U}_m^2\overline{C}_m$, is presented in *figure 21*. The production of turbulent flux $\overline{vc}$ by mean scalar and velocity gradients is counterbalanced by the fluctuating pressure field, limiting the turbulent flux growth, analogously to the pressure-strain correlation in the Reynolds shear stress transport equation.

The production term $(-\overline{v^2}\frac{\partial\overline{C}}{\partial r} - \overline{vc}\frac{\partial\overline{V}}{\partial r})$ and the pressure scrambling term $(-\frac{1}{\rho}\overline{c\frac{\partial p}{\partial r}})$ are dominant over the majority of the self-similar flowfield, compared to the advection term $(\overline{V}\frac{\partial\overline{vc}}{\partial r} + \overline{U}\frac{\partial\overline{vc}}{\partial x})$ and diffusion by velocity

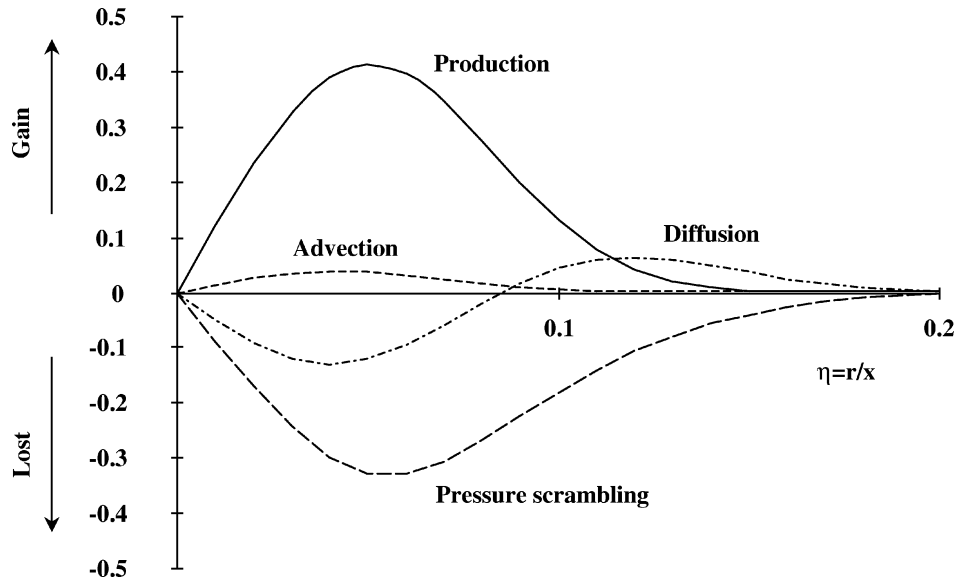

Figure 21. Budget of the turbulent scalar flux $\overline{vc}$ transport equation in normalized values. Production: $-\overline{v^2}\partial\overline{C}/\partial r - \overline{vc}\partial\overline{V}/\partial r$, diffusion: $-\partial\overline{v^2c}/\partial r - \overline{v^2c}/r + \overline{w^2c}/r$ and advection terms: $\overline{V}\partial\overline{vc}/\partial r + \overline{U}\partial\overline{vc}/\partial x$. The pressure scrambling term: $-1/\rho\overline{c\partial p/\partial r}$ is deduced from the other terms.

fluctuations ($-\frac{\partial\overline{v^2c}}{\partial r} - \frac{\overline{v^2c}}{r} + \frac{\overline{w^2c}}{r}$). The maximum production also corresponding to the pressure scrambling maximum is located at about $\eta = 0.06$, where the mean concentration gradient is the strongest.

According to Launder [12], and keeping the boundary layer approximation in mind, the pressure scrambling term may be written as:

$$\frac{1}{\rho}\overline{p\frac{\partial c}{\partial r}} = -C_{1c}\frac{\varepsilon}{k}\overline{vc} + C_{2c}\overline{vc}\frac{\partial\overline{V}}{\partial r}. \tag{12}$$

Considering that the approximation ($\overline{p\frac{\partial c}{\partial r}} \cong -\overline{c\frac{\partial p}{\partial r}}$) is valid, since turbulent diffusion due to pressure fluctuations ($\frac{\partial\overline{cp}}{\partial r}$) is neglected [12], the pressure scrambling term is given by:

$$-\frac{1}{\rho}\overline{c\frac{\partial p}{\partial r}} \cong -C_{1c}\frac{\varepsilon}{k}\overline{vc} + C_{2c}\overline{vc}\frac{\partial\overline{V}}{\partial r}. \tag{13}$$

The kinetic energy of the turbulence has already been determined and the dissipation rate is provided by the bibliographical data. The distribution of the mean radial velocity, also necessary here, has been determined by the continuity equation.

The two constants C_{1c} and C_{2c} can be adjusted using least-squares fit of the pressure-scrambling term (*figure 22*), as done earlier for the Reynolds shear stress transport. The calculated values are $C_{1c} = 2.78$ and $C_{2c} = 0.1$. Launder [12] obtained a different set of values ($C_{1c} = 3.2$ and $C_{2c} = 0.5$) with the use of Webster's [23] data collected in an homogeneous shear turbulent flow in presence of a linear temperature gradient. No conclusion about the differences in the numerical constants can be stated, since the jet flows are generally very sensitive to the injection conditions. It demonstrates only that the model for the pressure scrambling term works in such a flowfield.

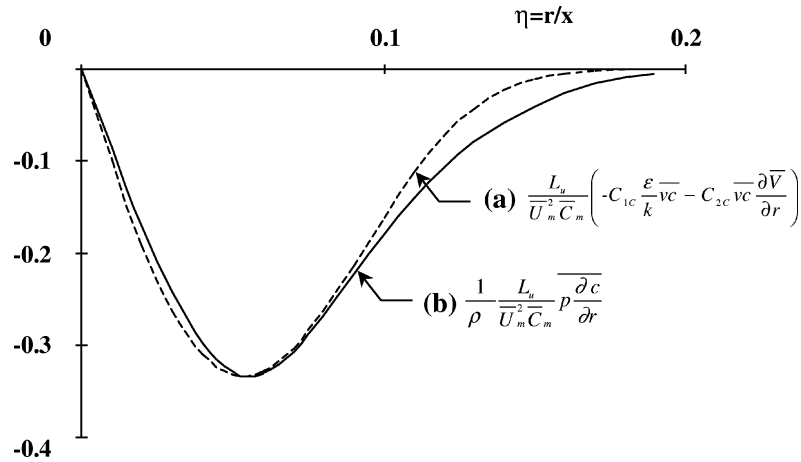

Figure 22. Closure model for the pressure scrambling term: (a) pressure scrambling term, and (b) closure model. Adjustment of the two constants C_{1C} and C_{2C} using least-squares fit.

4.3.4. Model for the turbulent transport

In the first approach, one can conclude from the budget of *figure 21* that the approximation production $\approx$ pressure scrambling is valid over the major part of the self-similar flowfield. It means that advection and diffusion terms can be neglected. It may be written as:

$$-\frac{1}{\rho}\overline{c\frac{\partial p}{\partial r}} \cong \overline{v^2}\frac{\partial \overline{C}}{\partial r} + \overline{vc}\frac{\partial \overline{V}}{\partial r}. \tag{14}$$

With the use of expression (13) for the pressure scrambling term, equation (14) yields the turbulent flux $\overline{vc}$:

$$\overline{vc} = -\frac{\Phi'_c \overline{v^2}\frac{\partial \overline{C}}{\partial r}}{\frac{\varepsilon}{k} + \Phi_c \frac{\partial \overline{V}}{\partial r}}, \tag{15}$$

where Φ_c and Φ'_c are combinations of the constants C_{1c} and C_{2c}:

$$\Phi_c = \frac{1 - C_{2c}}{C_{1c}}, \quad \Phi'_c = \frac{1}{C_{1c}}. \tag{16}$$

If the contribution of the radial velocity gradient is neglected, a simple turbulent diffusivity closure model can be obtained:

$$\overline{vc} = -D_t \frac{\partial \overline{C}}{\partial r}, \tag{17}$$

where $D_t = \frac{k}{\varepsilon}\Phi_c \overline{v^2}$ is a turbulent diffusion coefficient.

These two steps of description of the turbulent flux are illustrated in *figure 23* where the present measurements in comparison with equation (15) and equation (17) are reported. The better agreement is obtained with equation (15). However a moderate difference is observed between the simple turbulent diffusivity model (equation (17)) and the more complex one (equation (15)). A significant difference of about 15% on the maximum value and 8% on the maximum location, between the model of equation (15) and

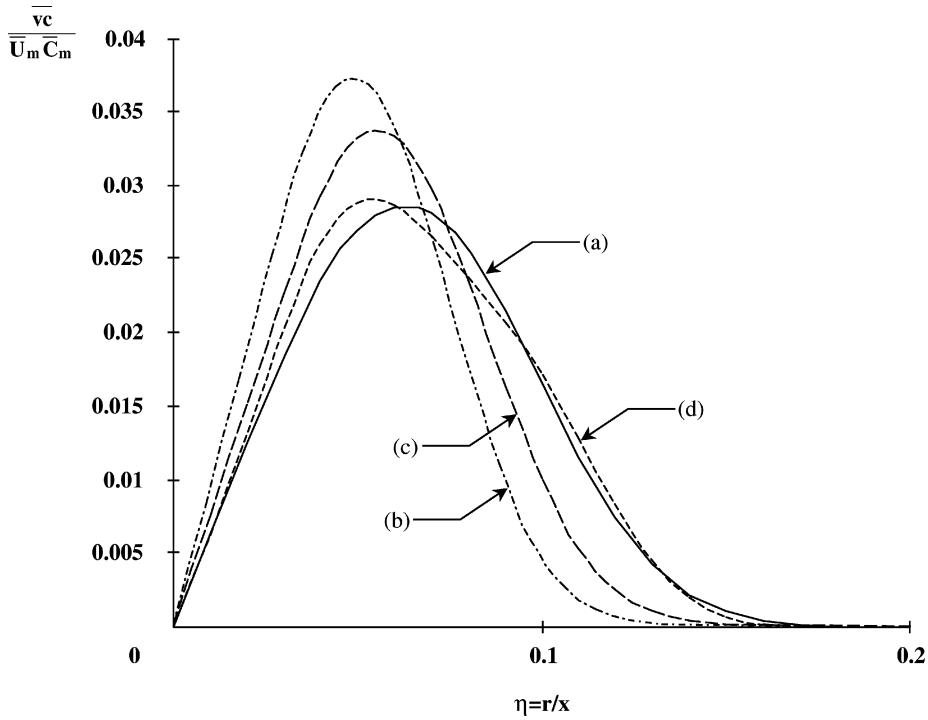

Figure 23. Comparison of models for the radial turbulent scalar flux $\overline{vc}$: (a) fit of the present measurements; (b) turbulent diffusivity model (equation (17)); (c) model of equation (15); (d) model of equation (20).

experimental data can be observed. This difference can be mainly attributed to the diffusion term which has been neglected. The next section is devoted to a model for the diffusion term.

4.3.5. Model for the diffusion term

The amplitude of the diffusion term can reach 30% of the production or pressure scrambling term (see *figure 21*). This term should be taken into account in order to improve the physical description of the turbulent transport.

The diffusion term is given in equation (7) by:

$$\textit{Diffusion} = -\frac{\partial \overline{v^2 c}}{\partial r} - \frac{\overline{v^2 c}}{r} + \frac{\overline{w^2 c}}{r}. \tag{18}$$

Both triple correlations $\overline{v^2 c}$ and $\overline{w^2 c}$ have the same order of magnitude, in order that the difference $-\overline{v^2 c}/r + \overline{w^2 c}/r$ can be neglected. A model for the gradient $\partial \overline{v^2 c}/\partial r$ is required.

A gradient type model for the triple correlation $\overline{v^2 c}$, proposed initially by Daly and Harlow [1], where axisymmetry and boundary layer hypothesis are considered, may be written as:

$$\overline{v^2 c} = -C_c \frac{k}{\varepsilon} \overline{v^2} \frac{\partial \overline{vc}}{\partial r}, \tag{19}$$

where C_c is a numerical constant.

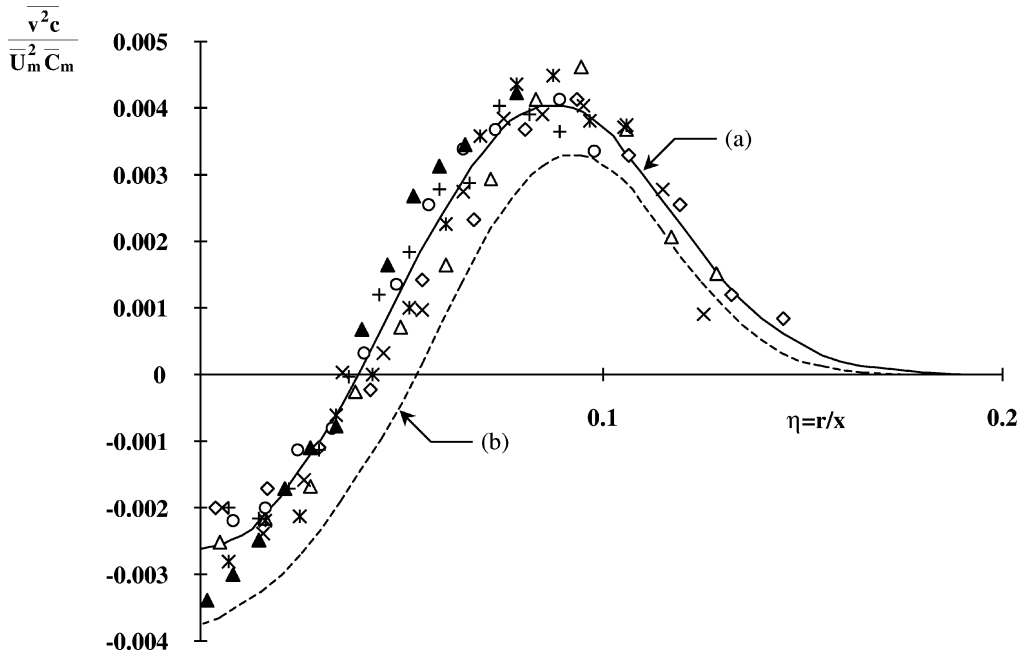

Figure 24. Distribution of the triple moment $\overline{v^2c}$ across the jet: (a) fit of the measurements and (b) comparison to the closure model. (See *figure 19* for the other symbols.)

With the help of the present measurements and data provided in the literature for the kinetic energy of turbulence dissipation rate ε, the adjusted constant C_c, is found to be 0.137 using a least squares fit.

The model and the experimental data for the $\overline{v^2c}$ profile are shown in *figure 24*. Although the fit is not perfect, the general trend of $\overline{v^2c}$ is respected and the maxima locations are in agreement.

Neglecting the advection term in equation (7) and using the model for the pressure scrambling and diffusion terms, the turbulent flux $\overline{vc}$ can be written as:

$$\overline{vc} = -\frac{\Phi_c\left(\overline{v^2}\frac{\partial\overline{C}}{\partial r} - C_c\frac{\partial}{\partial r}\left(\frac{k}{\varepsilon}\overline{v^2}\frac{\partial\overline{vc}}{\partial r}\right)\right)}{\frac{\varepsilon}{k} + \Phi_c\frac{\partial\overline{V}}{\partial r}}. \tag{20}$$

The good agreement between this more complete model and the experimental data can be observed in *figure 23*. It must be noted here that the turbulent flux $\overline{vc}$ has been calculated from the measurements in the modelisation of the triple correlation $\overline{v^2c}$. It demonstrates the adequacy and coherence of the different models which have been used for the pressure scrambling and diffusion term.

4.4. Turbulent Schmidt number

Figure 25 shows the normalized turbulent mass diffusivity ($\frac{D_t}{\overline{U}_m L_u}$). A comparison is carried out between the variable turbulent diffusivity model (equation (17)) and the complete model equation (20)) for the turbulent flux $\overline{vc}$. The better agreement with experimental results is obviously observed with the complete model. A moderate evolution of the turbulent diffusivity is found in the jet center region, where ($\frac{D_t}{\overline{U}_m L_u}$) attains a maximum, in the vicinity of $\eta = 0.065$. In the edges of this region, turbulent diffusivity decreases strongly to zero. It is in particularly good agreement with the thermal turbulent diffusivity reported by Chua and Antonia [8] for a free

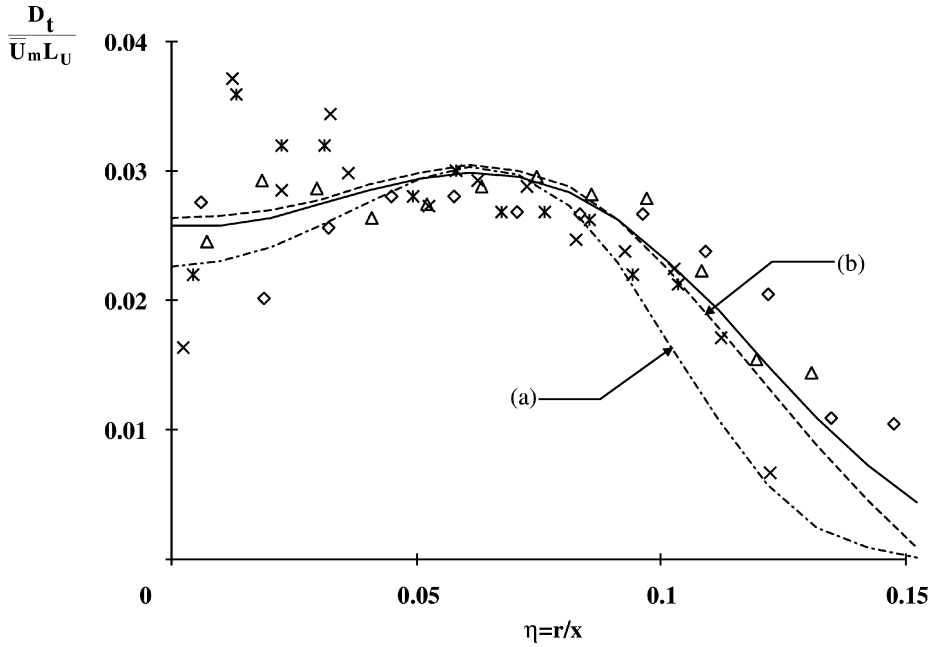

Figure 25. Distribution of the turbulent diffusivity $D_t = -\overline{vc}/\frac{\partial \overline{C}}{\partial r}$ across the jet and comparison to: (a) turbulent diffusivity model (equation (17)); (b) global model including the diffusion term (equation (20)); —— fit of the present measurements. (See *figure 19* for the other symbols.)

jet. The turbulent diffusivity averaged in the jet center region is about 0.03 in the present work and 0.033 in Chua and Antonia's [8].

On the one hand, the turbulent radial flux $\overline{vc}$ is here clearly higher than in Chua and Antonia's results, and on the other hand the spreading rate reduction tends to increase the concentration gradient across the jet. Consequently, turbulent diffusivity appears very similar to these determined by other authors for a free jet.

An usual way of relating variations of time averaged velocity and concentration across a turbulent shear flow is to define a turbulent Schmidt number, which can be defined as the turbulent momentum to mass diffusivity ratio:

$$S_{Ct} = \frac{\overline{uv}/\partial \overline{U}/\partial r}{\overline{vc}/\partial \overline{C}/\partial r}. \tag{21}$$

The turbulent Schmidt number, determined from the experimental data, is shown in *figure 26*. It can also be evaluated using the variable turbulent diffusivity model of equation (11) in combination with the variable turbulent diffusivity model of equation (17):

$$S_{ct} = \frac{\nu_t}{D_t} = \frac{\Phi}{\Phi_c} = 0.62. \tag{22}$$

It results to a constant Schmidt number in relatively good agreement with the values found in the jet center region, though not consistent with the general shape of S_{ct}. As seen in *figure 26*, the complete model for the turbulent flux provides better agreement and describes correctly the trend of the turbulent Schmidt number, which can be considered as constant in the center region for $0 \leqslant \eta \leqslant 0.08$ and decreases to zero in the mixing layer of the jet. Chevray and Tutu [7] found a similar almost constant value of the turbulent Prandtl number in the near field of the jet, while Chua and Antonia [8] measured a higher value of 0.81. The Schmidt number

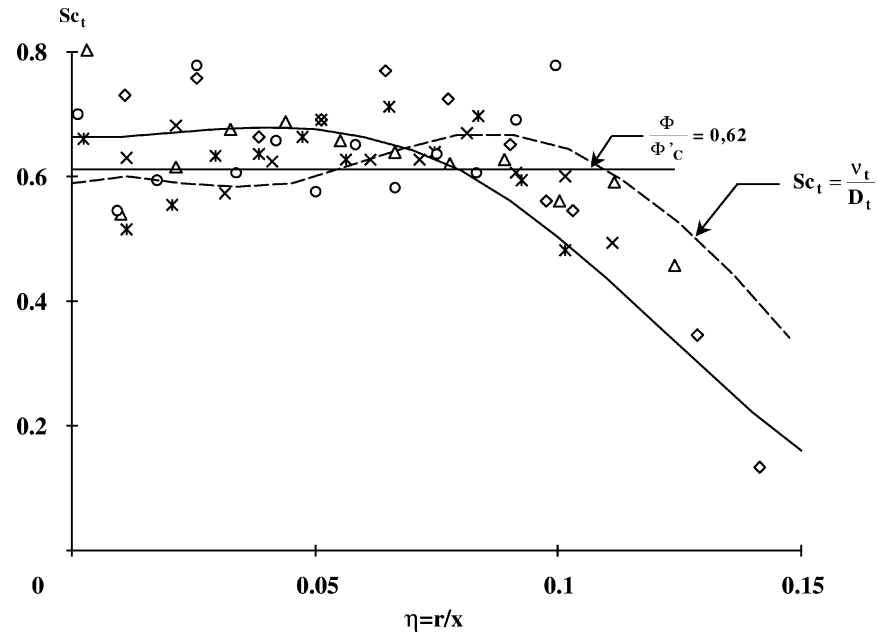

Figure 26. Distribution of the turbulent Schmidt number Sc_t across the jet. Comparison to $\Phi/\Phi'_c = 0.62$ and to the global model (equation (20)): - - - - —— fit of the present measurements. (See *figure 19* for the other symbols.)

results are consistent with the free jets results from the literature. Indeed, it has been shown that the co-flow has a minor effect on the turbulent diffusivity and turbulent viscosity factors.

5. Conclusions

Comprehensive turbulence measurements of both velocity and fluorescent tracer molecular concentration in a round turbulent jet of water discharging into a co-flowing stream have been presented in the self-similar range of the flowfield. Combined laser-induced fluorescence and 2D laser Doppler velocimetry are successfully used to measure correlations of both velocity and concentration fields. In spite of the presence of the co-flow, which should have a noticeable influence on the flowfield, the usual velocity turbulent characteristics, such as the second-order moments or Reynolds shear stress agree well with results reported in the literature for the free jet. Some differences in the magnitude of the longitudinal and radial turbulent fluxes, appearing higher in the present work than in the literature, are observed. The major visible effect of the co-flow is the jet spreading rate reduction, in comparison with the free jet case. Furthermore, the turbulent mixing between the clear water co-flow and the contaminated jet is enhanced, resulting in higher longitudinal and radial turbulent fluxes than in a free jet. On the other hand, the turbulent diffusivity and the turbulent Schmidt number appear fully consistent with those found in the literature for free jets. A qualitative agreement is found for the triple correlation $\overline{uv^2}$ and $\overline{uw^2}$ with the data of Hussein et al. [6] and Panchapakesan and Lumley [18], where a negative zone has been found. However, some disagreements in relation to the numerical values were observed. Some differences between the triple correlations $\overline{v^2c}$ and $\overline{w^2c}$ with the results of Panchapakesan and Lumley [10] are also pointed out, but these differences remain difficult to interpret, as the experimental conditions are quite different.

The budget for the Reynolds shear stress transport and the model initiated by Launder [12] for pressure-strain correlation allow a variable turbulent viscosity model $\nu_t = \frac{k}{\varepsilon}\Phi\overline{v^2}$ ($\Phi \approx 0.22$) to be considered.

A comparable variable turbulent diffusivity model, $D_t = \frac{k}{\varepsilon}\Phi_c\overline{v^2}$ ($\Phi'_c \approx 0.31$), can be defined if advection and diffusion terms and the contribution of the radial velocity gradient are neglected in the turbulent mass flux transport equation. The resulting Schmidt number is constant and equal to the ratio $\Phi/\Phi'_c \approx 0.62$.

Since this model appears not completely satisfactory, accounting for the diffusion term in the model, with an adequate model for the triple correlation $\overline{v^2 c}$, improves considerably the agreement with the measurements. The resulting turbulent Schmidt number is found to be almost constant and equal to about 0.62 in the center region and decreases strongly to zero in the mixing layer of the jet, and agrees well with the experimental results.

References

[1] Daly B.J., Harlow F.H., Transport equations in turbulence, Phys. Fluids 13 (1970) 2634–2649.
[2] Launder B.E., Reece G.J., Rodi W., Progress in the development of a Reynolds stress turbulence closure, J. Fluid Mech. 68 (1975) 537–566.
[3] Launder B.E., Samaraweera D.S.A., Application of a second-moment turbulence closure to heat and mass transport in thin shear flows. I – Two dimensional transport, Int. J. Heat Mass Tran. 22 (1979) 1631–1643.
[4] Hinze J.O., Van Der Hegge Zijnen B.G., Transport of heat and matter in the turbulent mixing zone of an axially symmetrical jet, Appl. Sci. Res. A1 (1949) 425–461.
[5] Wygnanski I., Fiedler H., Some measurements in the self preserving jet, J. Fluid Mech. 38 (1969) 577–621.
[6] Hussein J., Capp P., George K., Velocity measurements in a high-Reynolds number, momentum conserving, axisymmetric turbulent jet, J. Fluid Mech. 258 (1994) 31–75.
[7] Chevray R., Tutu N.K., Intermittency and preferential transport of heat in a round jet, J. Fluid Mech. 88 (1) (1977) 133–160.
[8] Chua L.P., Antonia R.A., Turbulent Prandtl number in a circular jet, Int. J. Heat Mass Tran. 33 (1990) 331–339.
[9] Dowling D.R., Dimotakis P.E., Similarity of the concentration field of gas-phase turbulent jets, J. Fluid Mech. 218 (1990) 109–141.
[10] Panchapakesan N.R., Lumley J.L., Turbulence measurements in axisymmetric jets of air and helium. Part 2: Helium jet, J. Fluid Mech. 246 (2) (1993) 225–247.
[11] Antonia R.A., Bilger R.W., An experimental investigation of an axisymmetric jet in a co-flowing air stream, J. Fluid Mech. 61 (1973) 805–822.
[12] Launder B.E., On the effects of a gravitational field on the turbulent transport of heat and momentum, J. Fluid Mech. 67 (3) (1975) 569–581.
[13] Lemoine F., Wolff M., Lebouché M., Simultaneous concentration and velocity measurements using combined laser-induced fluorescence and laser Doppler velocimetry, Exp. Fluids 20 (1996) 178–188.
[14] Lemoine F., Wolff M., Lebouché M., Experimental investigation of mass transfer in a grid-generated turbulent flow using combined optical methods, Int. J. Heat Mass Tran. 40 (1997) 3255–3266.
[15] Lemoine F., Antoine Y., Wolff M., Lebouché M., Mass transfer properties in a grid-generated turbulent flow: some experimental investigations about the concept of turbulent diffusivity, Int. J. Heat Mass Tran. 41 (1998) 2287–2295.
[16] Reid C.R., Prausnitz J.M., Poling B.E., The Properties of Gases and Liquids, McGraw-Hill, 1986.
[17] Antonia R.A., Satyaprakash B.R., Hussain A.K., Measurements of dissipation rate and some other characteristics of turbulent plane and circular jets, Phys. Fluids 23 (1980) 695–700.
[18] Panchapakesan N.R., Lumley J.L., Turbulence measurements in axisymmetric jets of air and helium. Part 1: Air jet, J. Fluid Mech. 246 (1) (1993) 197–223.
[19] Papanicolaou P.N., List E.J., Investigations of round vertical turbulent buoyant jets, J. Fluid Mech. 195 (1988) 41–391.
[20] Becker H.A., Hottel H.C., Williams G.C., The nozzle-fluid concentration field of the round turbulent free jet, J. Fluid Mech. 30 (2) (1967) 285–303.
[21] Hussein J., George K., Locally axisymmetric turbulence, Tech. Rep. 122, Turbulence Research Laboratory, University at Buffalo, SUNY, 1990.
[22] Champagne F.H., Harris V.G., Corrsin S., Experiments on nearly homogeneous shear flow, J. Fluid Mech. 41 (1970) 81.
[23] Webster C.A.G., An experimental study of turbulence in a density stratified shear flow, J. Fluid Mech. 19 (1964) 221.